Estimating Electric Field Distribution Generated by V2X Vehicular Communication in Urban Scenarios With Spatial Interpolation Techniques

Martina Benini, Silvia Gallucci, Samuel Goegebeur, Marta Parazzini, *Member, IEEE*, Wout Joseph, *Senior Member, IEEE*, and Gabriella Tognola

***Abstract*—This study assessed, for the first time, the feasibility of two interpolation techniques—o-kriging and co-kriging—to estimate the environmental electric field (E-field) in vehicle-to-everything communication at 5.9 GHz. Starting from a few E-field values obtained in an urban area, we designed an analytical approach based on (co-)kriging to estimate the E-field throughout the entire area accurately. We used *raytracing* to obtain E-field values used for training (12.5%) and validation. We evaluated our approach in four different vehicular scenarios with multiple transmitters (Txs) and obstacles (non-transmitting vehicles and buses). Co-kriging, besides the E-field values, also used Tx-Rx *distance* and *vehicle density* as additional inputs. The performance of (co-)kriging, measured by Pearson correlation and residuals, showed an accuracy of 89%–97%, depending on the number of Txs and obstacles. This approach reduced computational time by up to 87% compared to raytracing.**

***Index Terms*—Co-kriging, environmental electric field (E-field), o-kriging, spatial interpolation, urban scenario, vehicle-to-everything (V2X).**

I. Introduction

In THE era of technological evolution, a new branch of vehicular technologies called vehicle-to-everything (V2X) communication technologies is spreading in our daily lives. These innovative technologies are part of the intelligent transport system (ITS) concept [1] and rely on sophisticated wireless communication systems to provide more efficient, safe, and reliable mobility for road users and optimize traffic congestion and/or road conditions. V2X communication technologies are the backbone for the development of smart connected vehicles, enabling bidirectional communication between vehicles and the surrounding environment, including other vehicles [generating the so-called vehicle-to-vehicle communication (V2V) thanks to onboard units (OBUs)], infrastructures [vehicle-to-infrastructure communication (V2I) thanks to road-side units (RSUs)], pedestrians [vehicle-to-pedestrian communication (V2P)], and networks [vehicle-to-network communication (V2N)] [2], [3]. These technologies are based on two wireless communication protocols: the well-known IEEE 802.11p or ITS-G5 in Europe operating at 5.9 GHz [4], and the innovative cellular-V2X (C-V2X) based on LTE and Wi-Fi services with the expansion toward 5G functionalities (5G-V2X) [5], [6], [7], [8], [9].

The advent of these innovative technologies can lead to concerns among the population about involuntary exposure to radio frequency electromagnetic fields (RF-EMFs). To assess the exposure levels in the human body generated by V2X technologies, it is necessary to compute the electromagnetic (EM) fields [10]. From the literature, there exist two methods to estimate the EM fields in vehicular scenarios: 1) through experimental measures and 2) computational simulations [11]. Experimental measures generally have the advantage of measuring EM waves in realistic situations. Among computational simulations, instead, raytracing is one of the most common deterministic methods employed for simulating EM field propagation in vehicular connectivity scenarios (see e.g., [12], [13], [14], and [15]). It has the main advantage of providing an accurate estimation of the propagation of spatial and temporal multipath components of the EM waves from each transmitter and receiver. However, both of these two methods exhibit relevant drawbacks. Experimental measures are very expensive in terms of time and cost, and require a lot of implementation effort, while deterministic methods are very CPU-intensive and time-consuming, particularly when dealing with large vehicular scenarios. In this study, we aim to develop an analytical approach that, starting from E-field values obtained in a few positions of the area of interest, either from experimental measures or computational simulations, is capable of calculating the E-field in the remaining positions of the area while achieving computational efficiency and prediction accuracy at the same time. Our proposed approach is based on spatial interpolation techniques. Many spatial interpolation methods (both deterministic and stochastic) exist for data interpolation, such as nearest neighbor [16], spline [17], natural neighbor [17], inverse distance weighting (IDW) [16], [18], [19], and kriging [20]. In comparison to the other methods, IDW and kriging methods performed the best [16], [21], [22], [23]. Kriging is widely used for evaluating environmental E-fields because of its capability to provide, besides the estimated values, information about uncertainty on these values [24]. In the present work, we design an analytical approach based

Received 1 August 2024; revised 10 March 2025; accepted 12 May 2025. Date of publication 29 May 2025; date of current version 8 September 2025. This work was supported by the Project "EXPOAUTO–Cumulative Real Smart Car Exposure to Radio Frequency Electromagnetic Fields in People of Different Ages from New Technologies in Automotive Services and Connected Objects" [National Research Programme for Environmental and Occupational Health (PNR EST) Anses, 2020/2 RF/05]. *(Corresponding author: Martina Benini.)*

Martina Benini, Silvia Gallucci, Marta Parazzini, and Gabriella Tognola are with the Institute of Electronics, Computer and Telecommunication Engineering (IEIIT), Consiglio Nazionale delle Ricerche (CNR), 20133 Milan, Italy (e-mail: martinabenini@cnr.it).

Samuel Goegebeur and Wout Joseph are with the Department of Information Technology, IMEC, Ghent University, 9052 Ghent, Belgium.

Digital Object Identifier 10.1109/TAP.2025.3572608

TABLE I
COMPARISON WITH PREVIOUS STUDIES USING KRIGING INTERPOLATION TECHNIQUE FOR ENVIRONMENTAL E-FIELD ESTIMATION

References	Interpolation technique	EMF source	Objective	Scenario investigated
[25]	Kriging	WiFi @ 2GHz	Estimation of the environmental E-field	Indoor scenario
[26]	Kriging	Base Stations (100 kHz – 3 GHz)	Mapping of the environmental E-field	Urban scenario
[27]	Kriging	WiFi (88 MHz – 5.85 GHz)	Estimation of RF-EMF levels	Public transport, subway, home
[28]	Kriging	Base station @900 MHz, 1.8 GHz, 2.1 GHz	Surrogate models of the environmental E-field	Urban scenario
[29]	Kriging	WiF @2.45 GHz	Mapping of the environmental E-field	Indoor scenario
[30]	Kriging	LTE network	Interpolation of the E-field signal noise strength	Route around office building
[31]	Kriging	5G-V2X	Reconstruction of the radio environmental map of the received power	Analytical highway scenario
[32]	Kriging	5G-V2X	Reconstruction of the radio environmental map of the received power.	Analytical vehicular sub-urban scenario
Our study	Kriging & Co-kriging	V2X @5.9 GHz	Estimation of the environmental E-field	Vehicular urban scenario

on ordinary-kriging (o-kriging) and co-kriging for estimating environmental E-field values in realistic V2X vehicular urban scenarios, which include features such as roads, buildings, cars, and buses. Table I summarizes a list of studies that use kriging to estimate the environmental E-field generated by different EMF sources in order to provide a comparison with our study. As seen in Table I, previous studies applied the kriging interpolation technique to estimate environmental EMF in generic outdoor urban areas and indoor areas. For example, in [25], kriging was applied to EMF for spatial interpolation of the environmental E-field in an indoor scenario, showing how kriging can be used to speed up the field estimation process. In [26] and [27], kriging was used for the analysis and mapping of the E-field levels measured in an urban area, investigating the influence of sampling resolution [26] and on different microenvironments such as street, public transport, subway, and home [27]. Also, [28] used kriging to interpolate E-field values generated by base stations (BSs) (for telecommunication wireless, radio, and television broadcasting), and these data were used to build a surrogate model for the identification of hotspots, i.e., regions where the environmental E-field is significantly higher compared to the average. Martínez-González et al. [29] designed a method for estimating the EM environmental map in two different indoor scenarios based on the kriging interpolation technique, and Schießl et al. [30] used kriging to interpolate noisy measurements of the E-field signal strength from common smartphones. Moreover, as seen in Table I, no study has applied the kriging interpolation technique for the estimation of the environmental E-field generated by V2X communication in vehicular urban exposure scenarios. As a matter of fact, we found that in previous studies, kriging was generally applied to highway [31] and suburban environments [32] for the reconstruction of radio environmental maps (REMs) (Table I).

Besides kriging, we decided to consider another technique, i.e., the co-kriging technique, which is an extension of the o-kriging. While o-kriging estimates the E-field values taking into account only the primary features, i.e., the variable of interest (which in our application is the E-field), co-kriging has the advantage of considering, besides the primary feature, additional features (also called secondary features or covariables), i.e., characteristics specific to the scenario investigated. In principle, covariables can be useful to improve the accuracy of the o-kriging estimation [33]. To the best of our knowledge, co-kriging has never been applied to estimate RF-EMF exposure. As a result of this approach, we are able to investigate vehicular scenarios more quickly and easily than when only experimental measures or deterministic methods are used. Specifically, in this study, we used raytracing implemented on Remcom Wireless InSite to obtain the E-field values (denoted as true E-field values) generated by V2X technologies in a real urban area of the city center of Manhattan. As V2X communication technologies, we considered V2V and V2I communication technologies operated at 5.9 GHz [4]. To assess the performance of (co-)kriging, the different number of transmitting vehicles, i.e., OBU antennas (V2V) and RSU antennas (V2I), was considered. Some of the true E-field values obtained from raytracing were used for training the (co-)kriging algorithm, and the remaining values were used for validating its performance. In the co-kriging analysis, we considered as secondary features the geometrical characteristics of the environment specific to the vehicular scenario. Finally, the accuracy between the estimated and true E-field values was assessed by computing the Pearson correlation coefficient, and residual measures, such as root-mean-square error (RMSE), mean error (ME), and mean square deviation ratio (MSDR). In summary, the main contribution of this article is that, for the first time, two spatial interpolation techniques, i.e., o-kriging and co-kriging, were applied for the estimation of the environmental E-field in the specific domain of vehicular communication. In this article, we provide.

1) An evaluation of the performance of both o-kriging and co-kriging techniques.
2) A comparison of the accuracy of o-kriging and co-kriging.
3) An investigation of the robustness and stability of the co-kriging by varying the number of covariables used (i.e., characteristics of the scenario investigated) for estimating the E-field values.
4) A quantification of the computational time saved using the proposed approach compared to solely using the raytracing method.

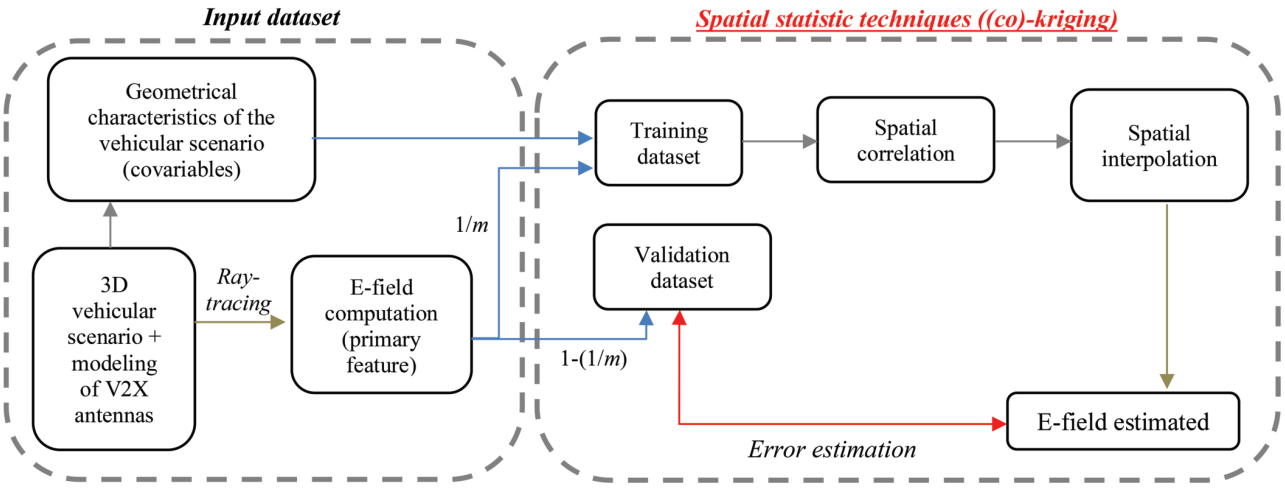

Fig. 1. Schematic representation of the proposed approach. Please note that the chart highlights the steps specifically used with the co-kriging technique. Indeed, while co-kriging used both primary feature and covariables (i.e., E-field and geometrical characteristics of the scenario) for training, the o-kriging made use only of the primary feature (E-field). In this chart, m is the refinement chosen; specifically, $1/m$ is the number of data used for training, and the remaining $(1 - 1/m)$ is the number of E-field data points used for validation (for details about the refinement, see Section II-B *"primary and secondary features"*).

II. Materials and Methods

From here on, for simplicity, we refer to the *environmental* E-field as just the E-field.

Fig. 1 represents the steps we followed for developing the approach. We employed a deterministic method, i.e., the *raytracing* technique, to obtain the E-field in a large area of a 3-D vehicular scenario. The E-field obtained (defined as the *primary feature*, i.e., the variable of interest) was used for training and validating (co-)kriging. Specifically, the o-kriging was trained considering only the E-field, while for co-kriging, it was considered the E-field together with geometrical characteristics of the environment (defined as *secondary features* or *covariables*) specific to the 3-D vehicular scenario. The two spatial interpolation techniques used a two-step process for estimating the E-field values, i.e., a spatial correlation analysis (to quantify the degree of spatial correlation of the data through the variogram) and a spatial interpolation analysis (for estimating the unknown E-field values based on the degree of spatial correlation previously found). The E-field values that were estimated by (co-)kriging were then compared to the true E-field values that were obtained by *raytracing* to compute prediction accuracy.

In Sections II-A–II-F, these steps will be explained in detail.

A. Deterministic Method

In this section, we analyzed in detail the steps performed in the first block, "*Input dataset*" in Fig. 1.

1) 3-D Vehicular Exposure Scenario: The vehicular scenario was modeled considering a realistic 3-D map of the city center of Manhattan. It comprises three road intersections of total dimension 170 × 230 m with multiple features typical of a real vehicular scenario, such as road terrain made of asphalt, buildings of varying sizes made of concrete, and different vehicles and buses. As V2X communication RF-EMF sources, we considered OBU antennas (to perform V2V communication) installed on vehicles (one per vehicle) and RSU antennas (to carry out V2I communication) installed on infrastructures such as streetlamps and traffic lights. To account for some variability in the vehicular scenario, we considered four exposure scenarios with different numbers and positioning of transmitting vehicles (i.e., OBU antennas) and RSU antennas.

Fig. 2 shows the top view of the four vehicular exposure scenarios considered. The scenarios are listed in order of increasing complexity.

1) *Scenario A:* One Tx vehicle (OBU) +1 RSU [Fig. 2(a)].
2) *Scenario B:* One Tx vehicle (OBU) +3 RSUs [Fig. 2(b)].
3) *Scenario C:* Three Tx vehicles (OBUs) +1 RSU [Fig. 2(c)].
4) *Scenario D:* Six Tx vehicles (OBUs) +1 RSU +7 non-transmitting vehicles (five cars and two buses) [Fig. 2(d)].

All vehicles and buses are static objects (i.e., not moving).

2) Modeling of OBU and RSU Antennas and Electromagnetic Properties of the Environment: OBU and RSU antennas were modeled as omnidirectional antennas, i.e., half-wave dipoles [15], [34], [35], [36], [37], [38], operating at 5.9 GHz with a bandwidth of 10 MHz [4], [39]. Each antenna operated with an input power of 33 dBm, i.e., the maximum allowable power in the EU [4], with a gain of 0 dBi.

The OBU antenna was placed on the roof of the car [40], [41] at a height of 1.7 m from the ground (one antenna per car), while the RSU antennas were placed next to the building façade 5 m away from the ground and tilted 10° toward the ground according to 3GPP protocol [39].

The dielectric properties of the objects present in the vehicular scenarios were assigned according to the ITU database [42] and literature data [43] (Table II).

3) E-Field Computation: To assess the E-field values for training and validating the (co-)kriging in the four realistic vehicular exposure scenarios (Fig. 2), we used the *raytracing* technique implemented on Remcom Wireless InSite [44]. The

Fig. 2. Top view of the four different vehicular exposure scenarios investigated. (a) Scenario A has 1 transmitting vehicle (OBU) and 1 RSU. (b) In scenario B, in addition to the EM sources of scenario A, we introduced another 2 RSUs. (c) Scenario C, in addition to scenario A, has 2 more OBUs. (d) Finally, scenario D is the same as scenario A, with 4 more OBUs and 7 obstacles (cars and buses). The white arrows point to the vehicles that are transmitting, while the white blocks on both sides of the roads represent the buildings. Please note that the green and red lines at the RSU are the *x*-axis and *y*-axis, respectively.

TABLE II

DIELECTRIC PROPERTIES OF THE OBJECTS PRESENT IN THE VEHICULAR SCENARIO. DHS: DIELECTRIC HALF-SPACE, OLD: ONE-LAYER DIELECTRIC, AND PEC: PERFECT ELECTRIC CONDUCTOR

Objects	Materials	Type	Conductivity (S/m)	Permittivity (adimensional)
Pavement/ Terrain	Asphalt	DHS	0	5.72
Buildings	Concrete	OLD	0.12	5.31
Hub Caps (car/bus)	Plastic	OLD	0.05	4.70
Lights (car/bus)	Plastic	OLD	0.05	4.70
Mirrors (car/bus)	Glass	OLD	0.23	6.27
Bumper (car/bus)	Plastic	OLD	0.05	4.70
Tired (car/bus)	Rubber	OLD	0.06	2.6
Body car/bus	Metal	PEC	/	/
Undercarriage	Metal	PEC	/	/

raytracing technique is a deterministic method based on two algorithms, i.e., geometric optics (GOs) and uniform theory of diffraction (UTD), for the evaluation of physical optics phenomena like reflection, refraction, and diffraction between each transmitter (Tx) and the receiver (Rx). The Txs are represented in our case by OBU and RSU antennas (previously described in Section II-A2), while as Rx we modeled a grid of Rxs on the *xy plane* of the vehicular scenario (dimension of 170×230 m) as isotropic antennas with a space distance of 3 m between each Rx. The Rxs were placed at a height of 1.5 m along the z-axis, i.e., the average head height of a female adult.

Among the many propagation models implemented on Remcom Wireless InSite, we made use of the X3D model, i.e., the recent one for the investigation of outdoor scenarios, which effectively combined the shooting and bounding rays (SBRs) method and image theory (IM) [44]. All vehicular scenarios were simulated first without the diffuse scattering (DS) phenomenon, considering only reflection, refraction, and diffraction effects. However, considering that Solomitckii et al. [45] demonstrated that the DS phenomenon can significantly impact EM wave propagation in urban areas in nonline-of-sight (NLOS), to better assess the performance

TABLE III
COMPUTATIONAL PARAMETERS SET FOR THE RAYTRACING SIMULATIONS

Parameters
Propagation model: X3D
Ray spacing: 0.2° [44]
Number of reflections: 6 [44]
Number of refractions: 0 [44]
Number of diffractions: 1 [44]
Received threshold: -250 dBm
DS model: Directive model [46]
Scattering factors (S): 0.45 [13][46][47][48]
Cross-polarized factor (K-pol): 0.4 [13][46][47][48]
Alpha: 4 [13][46][47][48]

of both o-kriging and co-kriging in estimating E-field values, we also took into account the DS phenomenon in EMF propagation. Because the DS is very time-consuming, we applied it only to scenarios A and D (i.e., the simplest and the most complex ones). Table III reports the computational parameters used during the raytracing simulations for the evaluation of the E-field values; all these parameters were demonstrated to accurately predict EM wave propagation in outdoor scenarios [44].

B. Primary and Secondary Features

As previously mentioned, o-kriging and co-kriging are interpolation techniques used for spatial estimation, with the main difference that, while o-kriging estimates the variable of interest based on the spatial correlation of a single variable, i.e., *primary feature*, co-kriging instead estimates data based on the spatial correlation of multiple variables, i.e., primary feature and *secondary features* (also called *covariables*). In our study, we identified the primary feature as the E-field (V/m), as it is the data that we aimed to estimate, and as covariables the geometrical characteristics specific to the vehicular exposure scenario investigated, which are correlated to the E-field. More precisely, we considered the following geometrical characteristics as covariables.

1) The Euclidean Distance Between Tx and Rx (d_Tx [m]): This feature is defined as the spatial distance between a reference Tx and each Rx. In our vehicular scenario, the Tx is represented by different OBU and RSU antennas [depending on the exposure scenarios considered (Fig. 2)], while the Rx is represented by a grid of points uniformly distributed along the scenario (see previous Section II-A3). This covariable has a negative correlation of −0.5 with the primary feature (E-field).

2) Vehicle Density [m]: This feature is defined as the mean distance from each Rx to the three closest vehicles (regardless of whether the vehicles are transmitters (Txs) or not). This feature was considered only in scenario D (Fig. 2), where more vehicles were presented in the scenario near each other. This covariable has a negative correlation of −0.76 with the E-field.

These geometrical features, together with the E-field values, are used as covariables and primary features for training the co-kriging in estimating E-field values (Fig. 1).

TABLE IV
COVARIABLES USED FOR CO-KRIGING ANALYSIS FOR EACH VEHICULAR EXPOSURE SCENARIO CONSIDERED. FOR EACH VEHICULAR SCENARIO, IN ADDITION TO THE COVARIABLES USED IN SCENARIO A, WE INTRODUCED ONE AT A TIME OTHER COVARIABLES CHOSEN SPECIFICALLY FOR THE DEGREE OF COMPLEXITY OF THAT SCENARIO

Vehicular exposure scenario	Covariable used
Scenario A	$d\_Tx_{vehicle1}$ + d_Tx_{RSU1}
Scenario B	Same of scenario A + d_Tx_{RSU2} + d_Tx_{RSU3}
Scenario C	Same of scenario A + $d\_Tx_{vehicle2}$ + $d\_Tx_{vehicle3}$
Scenario D	Same of scenario A + vehicle density

TABLE V
LIST OF ABBREVIATIONS OF THE COVARIABLES USED WITH THEIR CORRESPONDING DEFINITIONS

Abbreviation of the covariables	Definition
$d\_Tx_{vehicle1}$	Distance between the Tx vehicle 1 (Fig. 2A) and the Rxs.
d_Tx_{RSU1}	Distance between the RSU 1 (Fig. 2A) and the Rxs.
d_Tx_{RSU2}	Distance between the RSU 2 (Fig. 2B) and the Rxs.
d_Tx_{RSU3}	Distance between the RSU 3 (Fig. 2B) and the Rxs.
$d\_Tx_{vehicle2}$	Distance between the Tx vehicle 2 (Fig. 2C) and the Rxs.
$d\_Tx_{vehicle3}$	Distance between the Tx vehicle 3 (Fig. 2C) and the Rxs.

Table IV summarizes all the covariables used for each vehicular exposure scenario during the co-kriging analysis. Each covariable was chosen specifically for the degree of complexity of that vehicular scenario. In scenario A with two Txs, two corresponding covariables were used, i.e., the distance between each Rx and the Tx vehicle ($d\_Tx_{vehicle1}$) and RSU (d_Tx_{RSU1}). The covariables of scenario A were also considered in the other scenarios (B, C, and D), as the Txs of scenario A were present also in the other scenarios. In scenario B, compared to scenario A, two other RSU—RSU_2 and RSU_3 [Fig. 2(b)]—were introduced, and the corresponding covariables of the distance between the Rx and these two transmitting RSUs were introduced (i.e., d_Tx_{RSU2} and d_Tx_{RSU3}). In scenario C, two other Tx vehicles—$Tx_{vehicle2}$ and $Tx_{vehicle3}$ [Fig. 2(c)]—were introduced, and the corresponding distances between the Rx and these two transmitting RSUs were introduced in this case as covariables ($d\_Tx_{vehicle2}$ and $d\_Tx_{vehicle3}$). In scenario D (the most complex one), the *vehicle density* was considered as an additional covariable. For the sake of clarity, Table V reports the list of abbreviations of each covariable used, along with their corresponding definitions.

C. Training/Validating Dataset

The primary and secondary features previously extracted first underwent a preprocessing phase before being used for spatial analysis. Fig. 3 illustrates in detail the steps of the preprocessing analysis used here. Fig. 3 shows that we first removed from each array variable (primary and secondary features) the Rx points placed inside the buildings (or inside vehicles and buses), as we want to compute the

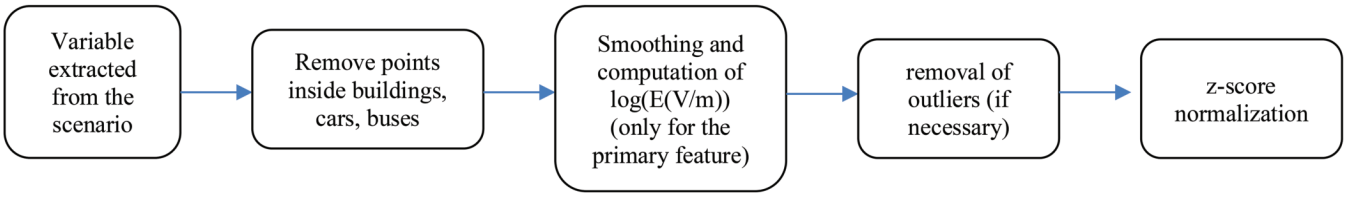

Fig. 3. Graphic representation of the preprocessing steps of the variable before being used as input for the spatial interpolation methods.

E-field distribution exclusively in the outdoor scenario. We also performed a smoothing of the E-field, considering as E-field value at the Rx point the mean of the surrounding four Rxs. Furthermore, since the spatial analysis techniques require normal distribution of the data, we express the E-field strength with a logarithmic transformation, log[E(V/m)]. This transformation turns the log-normal E-field distribution into a normal distribution that is proportional to the power density associated with the E-field. We then removed possible outliers (defined as the points that are not part of the normal distribution from the histogram). Finally, all the variables were then normalized with a z-*score normalization* to have a mean of zero and a variance of one by subtracting the mean and dividing by the standard deviation [48]. This step is necessary as kriging is an interpolation method based on the Gaussian process. If we define the primary feature of the E-field as $Z(x_i)$, where $i = 1, 2, 3, \ldots, n$, and for instance, the covariable of the Euclidean distance between Tx and Rx as $Y(x_j)$, where $j = 1, 2, \ldots, m$, then, the standardized variables are

$$Z_{std} = \frac{Z(x) - mean_Z}{\sigma_z} \quad \text{and} \quad Y_{std} = \frac{Y(x) - mean_Y}{\sigma_Y} \tag{1}$$

where σ represents the standard deviation of the variable.

The variables can now be used to characterize the spatial analysis. The part of the data from the primary feature was selected as training data, and the rest as validation data. The secondary features were considered only as training data. Specifically, in all the (co-)kriging analyses, we used a refinement of 8 for training and validation. This means that we considered as training data $1/8^{th}$ of the variable array, specifically, each 8^{th} element of the variable array (i.e., around 12.5%), and all the other remaining data were used for validation. This way, we obtained a total of around 205 training data and 1432 validation data, depending on the vehicular scenario considered.

D. E-Field Prediction With Spatial Techniques (O-Kriging and Co-Kriging)

In this study, we developed both o-kriging and co-kriging code using the software programming RStudio [50]. In Sections II-D1–II-D2, we describe how these two geostatistical methods work, dividing their process into two main phases: analysis of the spatial correlation and spatial interpolation (Fig. 1).

1) Spatial Correlation Analysis: The spatial correlation of the features is analyzed by calculating the experimental variogram and its fitting with a theoretical variogram [51]. The variogram is a graphic representation of the semivariance

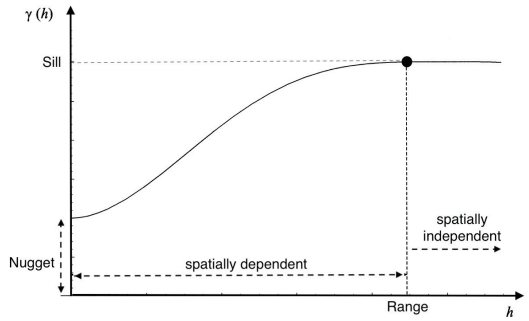

Fig. 4. Typical trend of the variogram highlighting *range*, *nugget* effect, and *sill* [51]. For simplicity, we refer to the variogram with γ(h) even if it is generally denoted as 2γ(h).

of the feature as a function of the lag distance, i.e., the distance between each pair of Rx. In particular, the experimental variogram is the plot of the observed E-field values, while the theoretical variogram is represented by a mathematical model that best fits all the data in the experimental variogram. While the o-kriging calculated only the experimental variogram of the primary features (i.e., E-field), the co-kriging developed an experimental variogram for each covariable considered. The equations for computing the experimental variogram by o-kriging and co-kriging are reported in Appendix A [see A1 (for o-kriging), and A2 and A3 (for co-kriging)]. The general behavior of the variogram is shown in Fig. 4. The variogram increases as the lag distance h (i.e., the distance between each pair of Rx) increases (according to A1, Appendix A). Indeed, when $h = 0$ the variance is zero and the spatial correlation is at its maximum as there is no difference between points that are compared with themselves. As h increases, the variance increases; and in turn, the spatial correlation decreases, because we are comparing points ever farther away, and it is unluckily that they are similar. After a certain lag distance h, called *range*, the variogram reaches a plateau, called *sill*, which represents the maximum amplitude of the variance (Fig. 4). This means that the *range* represents the maximum lag distance (h), after which there is no more correlation. Theoretically, for $h = 0$, the variogram should be zero. However, for $h = 0$, experimental variograms are always different from zero, giving rise to the *nugget effect* that could be caused by a possible physical phenomenon at a smaller scale or by some experimental or sampling error [24]. After obtaining the experimental variogram model, it is necessary to choose a mathematical model (that represents the theoretical variogram) to estimate the *range*, *sill*, and *nugget effect*. Generally, the commonly used theoretical models are the spherical model, Gaussian model, and exponential model. Depending on the vehicular scenario under investigation (Fig. 2),

we selected different theoretical models that best fit the corresponding experimental variogram obtained, i.e., we made use of the spherical and Gaussian models across the four different exposure scenarios.

The co-kriging, in addition to the variogram of the primary and secondary features [Appendix A (A2 and A3)], also calculated the cross-variogram (A4) through which it was possible to obtain the spatial relation between the multiple features (i.e., primary and secondary features). To model the three variograms of the co-kriging (two variograms and the cross-variogram) at the same time and ensure that the corresponding covariables are positive definite, the pseudo-cross-variogram was implemented, and the linear model of coregionalization (LMC) was used [52].

2) Spatial Interpolation Analysis: Both o-kriging and co-kriging performed an interpolation analysis based on the spatial correlation previously investigated through the variogram and cross-variogram to estimate the E-field values. In the o-kriging, the estimated data are expressed as a weighted linear combination of sample values, where the weights are determined based on the variogram model by minimizing the estimated variance. The co-kriging is based on the same rational as the o-kriging, but instead of providing weight coefficients only for the primary feature, it provides weight coefficients for each covariable considered. For details about the computation of the o-kriging and co-kriging weight coefficients used to estimate the unknown E-field values, see Appendix A (A5–A12).

E. Accuracy of E-Field Predicted

To assess the accuracy of the estimated E-field values by (co-)kriging, we calculated the Pearson correlation coefficient through linear regression and residual measures as follows.

1) *PearPearson correlation coefficient* (ρ) between the true E-field values (obtained from *raytracing*) and the estimated ones.
2) *RMSE* [V/m] of the residual is defined as the root mean square of the difference between the estimated E-field values and the true ones

$$RMSE = \sqrt{\frac{1}{N}\sum_{i=1}^{N}\left(E_{predict} - E_{validation}\right)^2} \ \text{[V/m]}.$$

We also computed the *RMSE relative to the maximum* E-field value obtained (rRMSE)

$$rRMSE = \frac{RMSE}{E_{max}} \cdot 100.$$

3) *MSDR of the Residuals:* This parameter provides detail about the spread/variability of the estimated E-field values compared to the variability of the true E-field values; it can be lower or higher than 1, where 1 indicates that the variability of the estimated E-field values perfectly matches the variability of the true data. It is expressed as

$$MSDR = 1 - \frac{\frac{1}{N}\sum_{i=1}^{N}\left(E_{predict} - E_{validation}\right)^2}{variance\left(E_{validation}\right)}.$$

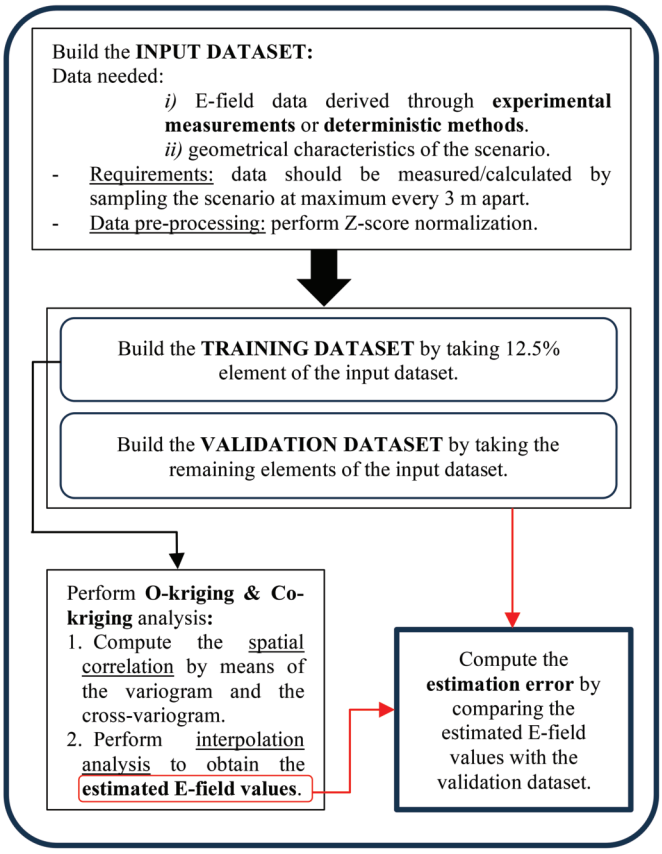

Fig. 5. Key aspects of the practical implementations of our approach.

4) *ME [V/m] of the Residuals:* This parameter represents the sum of the residuals divided by the number of elements in the array

$$ME = \frac{1}{N}\sum_{i=1}^{N}\left(E_{predict} - E_{validation}\right) \ \text{[V/m]}.$$

F. Practical Implementation

Fig. 5 summarizes the key aspects of the practical implementations of our proposed method, such as how to build the input dataset, the training/validation dataset, and the use of (co-)kriging to estimate E-field values.

III. Results

In Section III-A, we first present the results of co-kriging when two covariables were used. This analysis allows a comparison of the results between o-kriging and co-kriging and an assessment of how co-kriging performed varying the complexity of the vehicular scenario with fixed covariables. In Section III-B, the investigation of co-kriging was expanded by increasing the number of covariables chosen (Table IV). This analysis aims to validate the robustness and stability of the co-kriging technique to determine whether the different number of covariables has a positive, negative, or neutral impact on the quality of the data estimation. Finally, in Section III-C, a comparison of o-kriging and co-kriging was conducted, taking into account not only the "classic" ray propagation

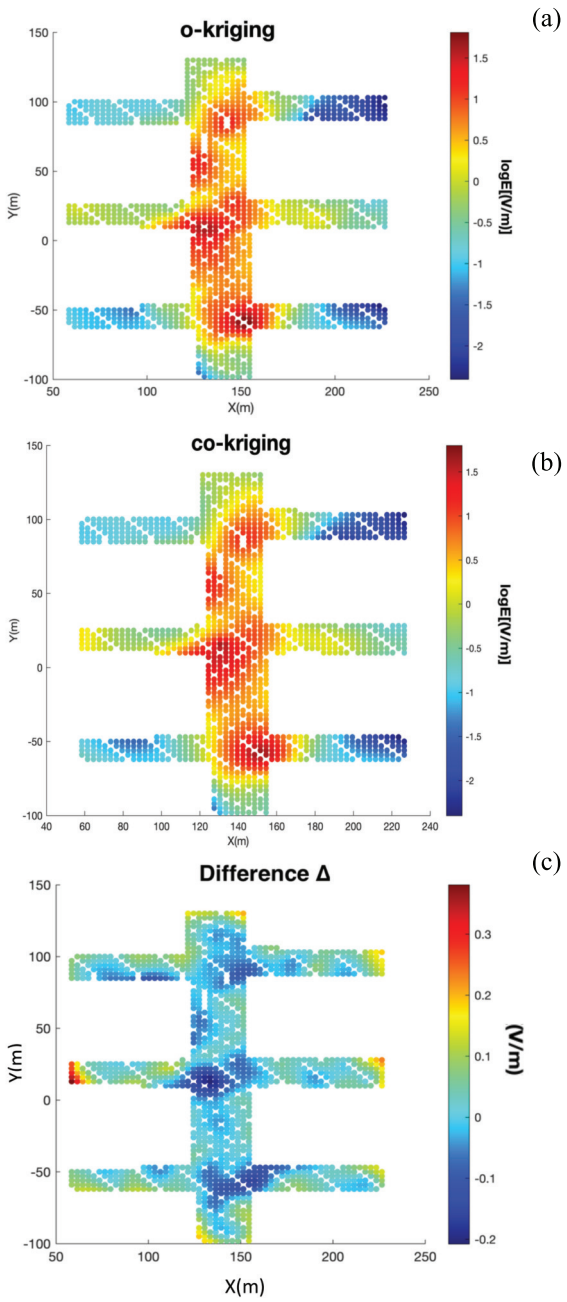

Fig. 6. (a) Distribution of the estimated log[E(V/m)] values obtained with both o-kriging and (b) co-kriging in scenario D. The white points are the training data and some white points are the ones removed from the analysis as they were inside buses/vehicles. (c) Difference $\Delta = \log E_{\text{co-kriging}} - \log E_{\text{o-kriging}}$ in the estimated logE between co-kriging (b) and o-kriging (a).

effects (reflection, refraction, and diffraction) in vehicular EM propagation, but also the DS effect.

A. Comparison Between O-Kriging and Co-Kriging With Two Covariables

Fig. 6(a) and (b) shows an example of the estimated log[E(V/m)] distribution obtained by o-kriging [Fig. 6(a)] and co-kriging [Fig. 6(b)] in the most complex scenario D. Fig. 6(c) shows the corresponding difference $\Delta = \log E_{\text{co-kriging}} - \log E_{\text{o-kriging}}$ between the estimated E-field values obtained with co-kriging and o-kriging. Fig. 6(c) shows

TABLE VI

RESIDUAL MEASURES COMPUTED FOR BOTH O-KRIGING AND CO-KRIGING AS A FUNCTION OF THE VEHICULAR EXPOSURE SCENARIOS. THE RESULTS REPORTED HERE FOR CO-KRIGING WERE OBTAINED CONSIDERING TWO COVARIABLES (TABLE IV, FIRST ROW)

Vehicular exposure scenario	O-kriging	Co-kriging (2 covariables)
Scenario A	ρ = 0.96 RMSE = 0.28 V/m rRMSE = 15.4% ME = 0.005 V/m MSDR = 0.91	ρ = 0.97 RMSE = 0.23 V/m rRMSE = 12.6% ME = -0.009 V/m MSDR = 0.94
Scenario B	ρ = 0.93 RMSE = 0.37 V/m rRMSE = 14.2% ME = 0.003 V/m MSDR = 0.86	ρ = 0.92 RMSE = 0.37 V/m rRMSE = 14.2% ME = 0.004 V/m MSDR = 0.86
Scenario C	ρ = 0.92 RMSE = 0.39 V/m rRMSE = 16.2% ME = 0.01 V/m MSDR = 0.85	ρ = 0.94 RMSE = 0.33 V/m rRMSE = 13.7% ME = 0.02 V/m MSDR = 0.89
Scenario D	ρ = 0.89 RMSE = 0.45 V/m rRMSE = 13% ME = -0.02 V/m MSDR = 0.80	ρ = 0.89 RMSE = 0.47 V/m rRMSE = 13.8% ME = -0.009 V/m MSDR = 0.77

that in most of the regions of the analyzed urban area, the differences between the two interpolation techniques are close to zero, with few regions where the predictions are slightly different; these regions are always placed at the boundaries of the scenario with co-kriging values slightly greater than o-kriging. The maximum difference found in the specific scenario was 0.38 V/m. Fig. 7 shows the linear regression between the estimated log[E(V/m)] values and the true log[E(V/m)] values for all the scenarios investigated for both o-kriging and co-kriging analysis. For each scenario, the Pearson correlation coefficient was the same for both o-kriging and co-kriging, revealing almost negligible differences between the two interpolation methods. Table VI lists the residual measures of the log[E(V/m)] values estimated along the grid of Rx in all the vehicular scenarios investigated in the present study. In all the vehicular scenarios (Table VI), both o-kriging and co-kriging estimated the E-field values with high Pearson correlation coefficients and very low residuals. More specifically, for both o-kriging and co-kriging, the Pearson correlation coefficients ranged from 0.89 to 0.97 among the vehicular exposure scenarios, with the highest ρ found in the simplest scenario (scenario A with 2 Txs) and the lowest one in the most complex scenario (scenario D with 7 Txs and many obstacles), as expected. The RMSE followed the same behavior, with its lowest value of 0.28/0.23 V/m in the simplest scenario A and the highest one of 0.45/0.47 V/m in the most complex scenario D. The rRMSE of o-kriging and co-kriging, across the different scenarios, are almost similar, with a mean of 15% in o-kriging and 13.5% in co-kriging.

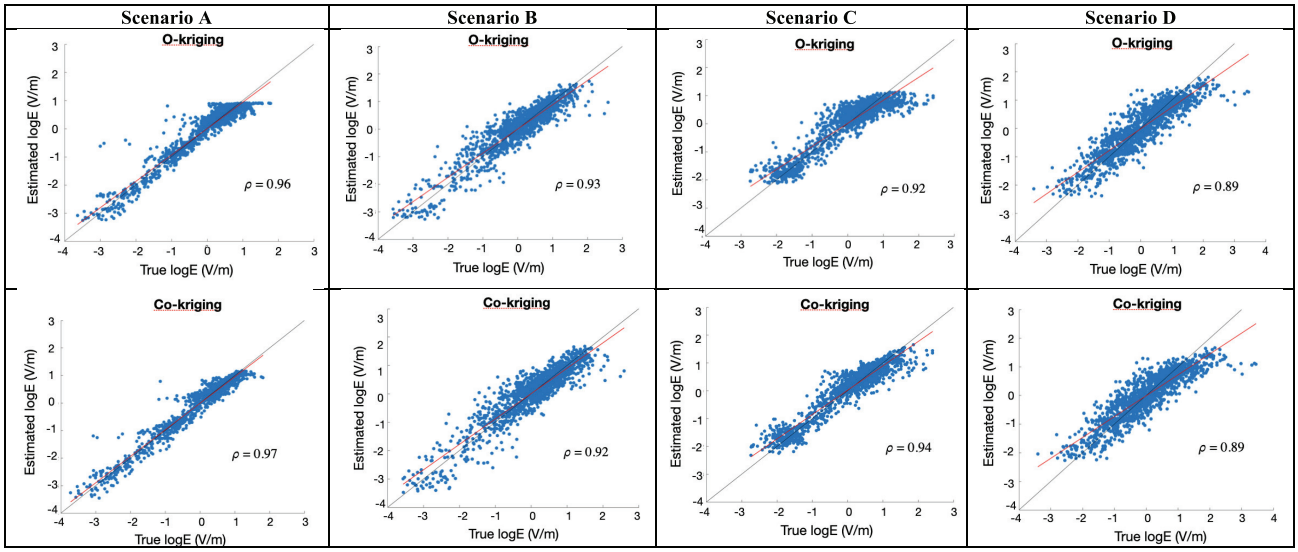

Fig. 7. Linear regression analysis for E-field obtained with o-kriging (top) and co-kriging (bottom) in all the scenarios investigated. The logE values are standardized with z-score normalization.

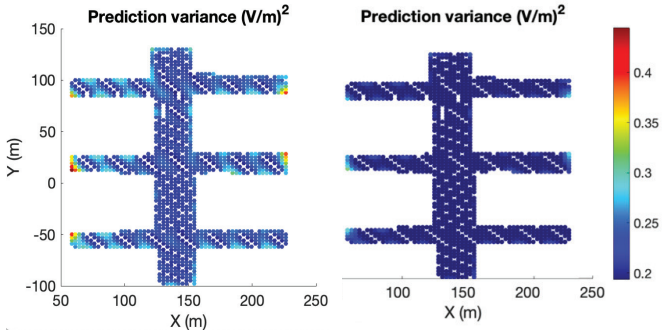

Fig. 8. Example of the prediction variance $(V/m)^2$ obtained with o-kriging **(left)** and co-kriging **(right)** in scenario D.

Generally, the ME of the residuals was almost zero in all the scenarios, and the MSDR of the estimations compared to the true values was generally lower than 1, meaning that the estimations made by (co-)kriging are less variable than the true values. However, this is to be expected, as kriging is a smoothing estimator. It is interesting to note that, even if the accuracy slightly decreases as the complexity of the vehicular exposure scenario increased, the rRMSE values between the complex (scenario D) and the simple scenarios (scenario A) were fairly constant both in o-kriging (13% versus 15.4%) and co-kriging (13.8% versus 12.6%). This suggests that both o-kriging and co-kriging provide a good estimation of the E-field even in complex vehicular scenarios. Despite co-kriging making use of covariables to "theoretically" improve prediction accuracy, in practice, as shown in Table VI, the quality of the prediction of co-kriging was similar to that of o-kriging (with slightly better performance in co-kriging).

To delve into the analysis of the comparison between o-kriging and co-kriging techniques, we analyzed the *prediction errors* [also called *prediction variance* or *kriging variance*, see Appendix B (A7)], which define the quality of the interpolation analysis by computing the local estimation error. Fig. 8 shows an example of the *prediction variance* for o-kriging (Fig. 8 left) and co-kriging (Fig. 8 right) in scenario D. As seen in Fig. 8, o-kriging had higher prediction variance compared to co-kriging, i.e., on average +28% than co-kriging. The prediction variance was generally lower (in the order of 0.2 V^2/m^2) close to the points used for training (the white points in Fig. 6) and increased up to +15% with distance from these points. In both o-kriging and co-kriging, the corresponding prediction variance values higher than the 99th percentile are placed at the edge of the scenario, more precisely in the corners of the streets. Fig. 9 represents the boxplot distribution of the *prediction variances* obtained with both techniques in all the different vehicular exposure scenarios investigated. The *prediction variances* obtained with co-kriging were on average from 2 to 15 times lower than those obtained with o-kriging in all the scenarios. This is because co-kriging considers additional information provided by covariables, increasing the confidence in the prediction and reducing the *prediction variance*. The higher *prediction variance* in o-kriging is reflected in its slightly lower accuracy in predicting E-field exposure compared to co-kriging (Table VI). However, we state again that the difference between the results from both methods is very small.

B. Co-Kriging Analysis With More Than Two Covariables

In this section, we investigate the robustness and stability of the co-kriging interpolation technique when more than two covariables are used. Table VII shows the Pearson correlation and residual measures when more than two covariables in the co-kriging analysis were considered. Specifically, we introduced the covariables previously shown in Table IV (see also Table V for definitions of the covariables). From Table VII, it is evident that an increased number of covariables in the co-kriging analysis did not improve the accuracy in estimating E-field values. Generally, the introduction of other covariables in addition to those used in scenario A brought only a marginal improvement in the correlation of 0.03%. Increasing the number of covariables resulted in a decrease in the *prediction variance* values. Therefore, while adding more covariables

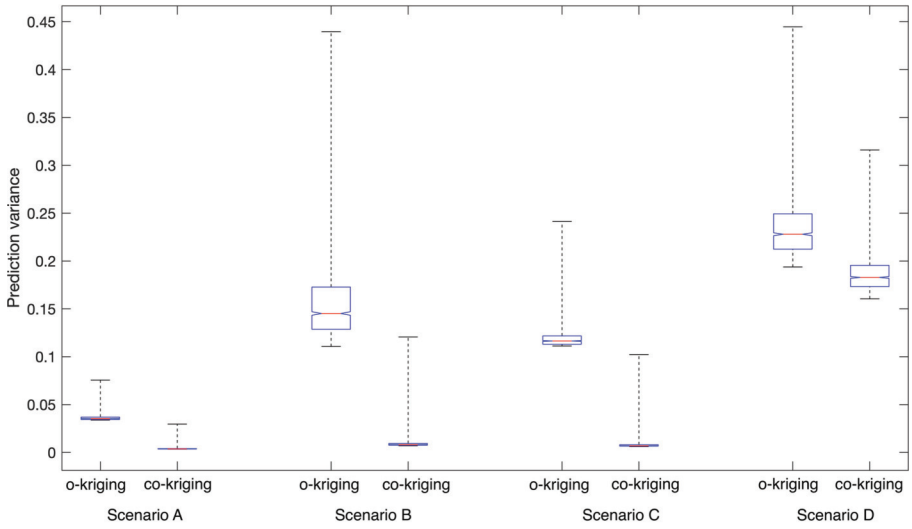

Fig. 9. Boxplot of the prediction variance $(V/m)^2$ of o-kriging and co-kriging in each exposure scenario. The upper and lower whiskers represent the maximum and minimum of the predicted variance, respectively; the bottom and top edges of the box are the 25th and 75th percentiles, respectively, and the red mark line in the center of the box indicates the median.

TABLE VII

RESIDUALS OBTAINED WITH CO-KRIGING IN SCENARIOS B, C, AND D WHEN MORE THAN TWO COVARIABLES WERE USED. THE COVARIABLES WERE ALREADY DESCRIBED IN TABLES IV AND V

			Diagnostic measures				
Vehicular exposure scenario	Number of covariables	Covariables (see Table V)	Pearson correlation coefficient	RMSE (V/m)	rRMSE	ME (V/m)	MSDR
Scenario B	3	Same of scenario A + d_Tx_{RSU2}	0.92	0.39	15%	0.006	0.84
	4	Same of scenario A + d_Tx_{RSU2} + d_Tx_{RSU3}	0.92	0.39	15%	0.005	0.84
Scenario C	3	Same of scenario A + $d\_Tx_{vehicle2}$	0.94	0.33	13.7%	0.018	0.9
	4	Same of scenario A + $d\_Tx_{vehicle2}$ + $d\_Tx_{vehicle3}$	0.94	0.33	13.7%	0.016	0.9
Scenario D	3	Same of scenario A + vehicle density	0.89	0.46	13.3%	-0.02	0.78

reduced prediction variance, it did not significantly enhance the prediction accuracy. This means that for the analyzed vehicular exposure scenarios, two covariables (defined as the distance between the Tx vehicle/RSU and the Rx), were enough to estimate E-field values with high accuracy.

C. DS Effect

In this section, we demonstrate the validity of these two spatial techniques when DS is applied for the estimation of E-field values in vehicular scenarios. From literature, the DS effect can significantly impact EM wave propagation in urban areas, where buildings and obstacles cause multiple scattering paths in NLOS conditions, especially at high frequencies [45]. For this reason, it is necessary to consider the scattering multipaths component when computing the E-field values. However, simulating the DS rays in deterministic methods exponentially increases the computational time. In addition, the spatial analysis of (co-)kriging can be more complicated due to the presence of these multiple paths. Hence, assessing the performance of (co-)kriging in estimating the E-field values with the DS effect has a relevant impact both in terms of validating the two spatial techniques and saving computational time.

D. Prediction Accuracy Considering DS Effect: O-Kriging and Co-Kriging With Two Covariables

Table VIII shows the measures of prediction accuracy of o-kriging and co-kriging considering the DS effect. For the sake of clarity, in Table VIII, we reported, besides the accuracy obtained considering the DS effect, also those obtained without DS, as already shown in Table VI. To limit computational time, when considering the effect of DS, we evaluated the prediction accuracy in scenarios A and D, i.e., the simplest and the most complex ones, respectively. Co-kriging was performed using the same two covariables of scenario A (Table IV, first row). From Table VIII, it is seen that the accuracy of o-kriging and co-kriging is also high when DS was considered, with no relevant difference when DS was not applied (Table VI). Only

TABLE VIII

RESIDUAL MEASURES OF O-KRIGING AND CO-KRIGING IN SCENARIOS A AND D WHEN THE DS EFFECT WAS APPLIED FOR THE ESTIMATION OF E-FIELD VALUES IN RAYTRACING SIMULATIONS. THE RESULTS REPORTED HERE FOR CO-KRIGING ANALYSIS WERE OBTAINED CONSIDERING TWO COVARIABLES (TABLE IV, FIRST ROW). FOR THE SAKE OF CLARITY, WE ALSO REPORTED THE RESIDUAL MEASURES OBTAINED WITHOUT DS FROM TABLE VI

Vehicular exposure scenario	O-kriging		Co-kriging (2 covariables)	
	With DS	Without DS (Table VI)	With DS	Without DS (Table VI)
Scenario A	ρ = 0.96 RMSE = 0.27 V/m rRMSE = 12.5% ME = 0.02 V/m MSDR = 0.92	ρ = 0.96 RMSE = 0.28 V/m rRMSE = 15.4% ME = 0.005 V/m MSDR = 0.91	ρ = 0.97 RMSE = 0.23 V/m rRMSE = 10.7% ME = 0.02 V/m MSDR = 0.94	ρ = 0.97 RMSE = 0.23 V/m rRMSE = 12.6% ME = -0.009 V/m MSDR = 0.94
Scenario D	ρ = 0.89 RMSE = 0.46 V/m rRMSE = 12.7% ME = -0.03 V/m MSDR = 0.78	ρ = 0.89 RMSE = 0.45 V/m rRMSE = 13% ME = -0.02 V/m MSDR = 0.80	ρ = 0.86 RMSE = 0.51 V/m rRMSE = 14.2% ME = 0.04 V/m MSDR = 0.73	ρ = 0.89 RMSE = 0.47 V/m rRMSE = 13.8% ME = -0.009 V/m MSDR = 0.77

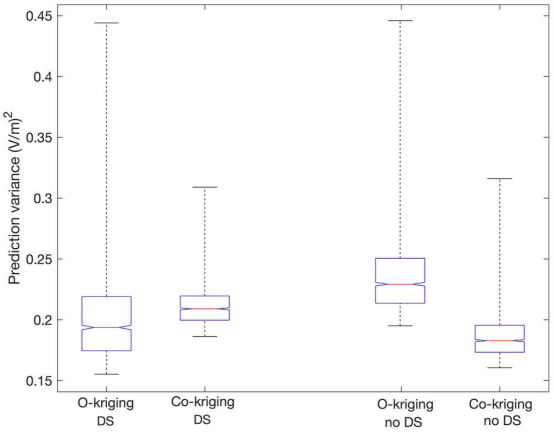

Fig. 10. Boxplot of the prediction variance distribution in scenario D with o-kriging and co-kriging when the DS was considered. For the sake of clarity, we also reported the boxplot obtained without DS, as already shown in Fig. 9. The upper and lower whiskers represent the maximum and minimum, respectively; the bottom and top edges of the box are the 25th and 75th percentiles, respectively, and the red line in the center of the box indicates the median.

for co-kriging in scenario D, the performance with DS slightly decreased compared to the co-kriging simulation without DS (Table VI). Indeed, ρ decreased from 0.89 to 0.86, the rRMSE and ME increased, and the MSDR decreased, meaning that the estimated data are less variable than what they should be. Fig. 10 shows the comparison between the *prediction variance* obtained with o-kriging and co-kriging in scenario D, which is the one that shows more differences between o-kriging and co-kriging when DS was considered. As seen in Fig. 10, differently from the case without DS, where co-kriging had lower prediction variance, here, with the DS effect, the *prediction variance* is on average slightly higher in co-kriging than in o-kriging [except for the maximum value (Fig. 10)]. This resulted in lower accuracy of the co-kriging when the DS is considered compared to o-kriging.

E. Co-Kriging Analysis With More Covariables

In this section, we analyze the prediction accuracy and the robustness of co-kriging in estimating E-field values when considering the DS effect and when using three covariables (see Table IV, scenario D) instead of only two for scenario D.

We found that the Pearson correlation coefficient was 0.88, RMSE was 0.47 V/m, rRMSE was 13%, ME was −0.02 V/m, and MSDR was 0.77. From these results, we can see that the accuracy of co-kriging slightly improved because of the use of three instead of two covariables. The introduction of the third covariable decreased the *prediction variance*, resulting in this case in an increase in the performance of the co-kriging, with a Pearson correlation coefficient higher [from 0.86 (Table VIII) to 0.88] and lower residual measures. This means that when we use the co-kriging spatial interpolation technique for estimating E-field values by considering also the DS effect, more than two covariables are useful to obtain a more accurate result. However, the co-kriging still does not perform better than the o-kriging.

IV. DISCUSSION

This study aimed to design and validate an interpolation approach for the estimation of E-field values in realistic V2X vehicular communication scenarios that comprise buildings, roads, vehicles, and buses. More specifically, we estimated the E-field values in all the positions of an area of interest by means of interpolation techniques (o-kriging and co-kriging) by starting from E-field values obtained at a few positions in the area. In this study, we used a *raytracing* deterministic method to obtain the E-field values in the area of interest. Part of these values were used for training; the remaining for validating the proposed approach. This is the first study where o-kriging and co-kriging were applied to estimate E-field values generated by V2X vehicular communication technologies in a generic urban setting. While o-kriging has been previously applied to estimate E-field values in generic urban (e.g., [28]) or indoor (e.g., [29]) scenarios, it has never been used specifically for E-field estimation in V2X communication. To the best of our knowledge, co-kriging has never been applied to estimate E-field values in an urban setting, either from generic wireless communication or specifically from vehicular communication.

TABLE IX
COMPARISON OF OUR METHOD WITH TRADITIONAL RAYTRACING TECHNIQUE AND EMPIRICAL MODELS TO COMPUTE EMF PROPAGATION IN VEHICULAR SCENARIOS

Techniques	Advantages	Disadvantages
Our method	High accuracy (89%-97%) and very low computational time (3-4 min)	It may not be so accurate in extensive scenarios (in the order of a few km^2)
Raytracing approach	High accuracy	It is required detailed modeling of the environment and high computational time (for our scenario without DS simulations take 30 min)
Empirical models	Good/high accuracy	Limitation in adapting to a new scenario

In the present study, the proposed approach was applied to different exposure scenarios of increasing complexity with increasing numbers of Tx and obstacles like cars and buses.

We compared o-kriging and co-kriging accuracy and tested the robustness of the co-kriging analysis by varying the number of covariables. As a general remark, we found that both o-kriging and co-kriging provide accurate estimates of the environmental E-field. With the proposed approach, we could estimate the E-field in the analyzed urban area using only $1/8^{th}$ of the total E-field samples of the area; this way, we could save up to 87% of the computational time required to run raytracing simulations on all the points of the area.

Both o-kriging and co-kriging provide high accuracy in estimating E-field values in the analyzed vehicular exposure scenarios. The correlation between estimated and true E-field values was consistently high across different vehicular scenarios, ranging from 89% in the most complex scenario to 96%–97% in the simplest vehicular scenario. The RMSE relative to the maximum was generally low, ranging from 13% to 16.2% with o-kriging and 12.6%–14.2% with co-kriging; the RMSE follows the same trend as the relative RMSE, showing low values. The MEs of the residuals were very low, on the order of 10^{-2}–10^{-3} V/m, and the MSDR was always below 1. It is interesting to note that, even when increasing the complexity of the vehicular exposure scenario—i.e., by considering multiple transmitting vehicles, RSUs, and many obstacles (cars and buses)—the performance remained generally high. Despite co-kriging using covariables to "theoretically" improve prediction compared to o-kriging, in practice, we did not find relevant differences in terms of accuracy and residual measures between o-kriging and co-kriging in the analyzed exposure scenarios. Thus, these results seem to suggest that at least for vehicular exposure scenarios involving V2X sources, such as vehicles and road infrastructures, o-kriging and co-kriging provide almost similar results. This means that we can estimate E-field values by just using o-kriging (the simplest approach between the two), which has an accuracy between 89% and 96%. We found that the use of additional covariables in co-kriging had almost no impact on the prediction accuracy.

Thanks to its high accuracy and low computational time and cost, with our approach, it is possible to overcome the main limitations of solely using *raytracing* or empirical models. Table IX compares the advantages and disadvantages of approaches based on raytracing and empirical modeling with our approach for applications in vehicular communication exposure scenarios.

The performance of these two spatial interpolation techniques was also tested in the case in which the contribution of the DS effect was considered. It is known from the literature that the DS effect has a relevant contribution to the E-field generated in urban areas, where the presence of rough surfaces (in buildings, roads, and pavement) can significantly impact EM wave propagation in NLOS regions [45]. We found that (co-)kriging reliably estimated E-field values even when the scattering effect of rays is taken into account. Generally, we did not find differences in terms of correlation and residual between the estimated E-field values and the true ones, compared to when DS was not applied. Only co-kriging with two covariables, in the most complex scenario D, showed a slight decrease in accuracy with higher residuals. In this case, co-kriging has more difficulties in estimating the additional scattering rays than o-kriging. Nevertheless, the introduction of a third covariable in the co-kriging analysis with DS slightly improved the accuracy (from 86% to 88%).

O-kriging has not previously been applied to estimate EMF generated by V2X communication technologies in vehicular scenarios. Thus, it is not possible to make a direct comparison between our study and the previous ones. Nevertheless, it might be interesting to make a quantitative comparison of the accuracy of o-kriging obtained in this study with that from other studies where o-kriging has been used to estimate EMF generated by other wireless technologies, such as Wi-Fi [25], [29], BS for communication, radio, and television [21], [26], [28], [57]. For a better comprehension, Table X illustrates a comparison between our results and those from other studies mentioned above. Specifically, in [21], kriging was used to map the E-field in an outdoor urban area in Caracas, while in Aerts et al. [28], kriging was used to generate maps of the RF-EMF exposure in an extensive urban area of Ghent. Azpurua and Ramos [21] and Aerts et al. [28] collected the environmental E-field values used for training the o-kriging with experimental measures. For a comparison with our results, we related the mean absolute error (MAE) and the mean square error (MSE) found by [21] (i.e., 0.74 and 0.73 V/m, respectively), to their maximum E-field value (i.e., 2.65 V/m), obtaining a relative MAE of 28% and a relative MSE of 27.5%. We obtained a lower relative MAE, i.e., ranging from 10% to 12%, and a lower relative MSE, i.e., between 4.4% and 6.3%. Similarly, Aerts et al. [28] obtained a correlation

TABLE X
COMPARISON BETWEEN OUR APPROACH WITH PREVIOUS ONES BASED ON O-KRIGING AND CO-KRIGING

		Scenario investigated		Parameters investigated			
References	**Interpolation techniques used**	**Type**	**Dimension [km^2]**	**Correlation**	**RMSE**	**MSE**	**MAE**
Our study	o-kriging	vehicular	0.039	0.89-0.96	13% - 16.2%	4.4% - 6.3%	10% - 12%
	co-kriging			0.89-0.97	12.6%- 14.2%	3% - 6.3%	10% - 13.3%
[21]	o-kriging	urban	2.64	N.A	N.A	27.5%	28%
[28]	o-kriging	urban	1	0.73	N.A	N.A	N.A
[29]	o-kriging	indoor	0.009	N.A	4.2%	N.A	3.9%

*N. A: not available

of 0.73, which is lower than what we obtained, even in our most complex vehicular scenario, i.e., 0.89. The differences from our results compared to those of [21] and [28] could be attributed to the characteristics of the scenarios, such as the dimension of the scenario, and the relative position between the Tx and Rx. Indeed, in our study, we investigated an area of 0.039 km^2, which is smaller compared to the larger dense urban area of 2.64 km^2 investigated in [21] and 1 km^2 of [28]. In a smaller area, the propagation paths interact less with the environment, resulting in E-field values that change more gradually and exhibit lower variability compared to those generated in larger and denser areas. In addition, in [21] and [28], the Tx was a rooftop-mounted BS. Consequently, most of the Rxs (located at a height of 1.5 m) are in NLOS conditions, which means that a high number of interactions between the propagation paths and the environment are needed to reach the Rx. On the contrary, in our study, OBU and RSU antennas are placed at a height (1.7 and 5 m, respectively) similar to that of the Rx (1.5 m), which means that most of the Rxs were in a line-of-sight (LOS) condition. Therefore, being in LOS, less interactions occur, and the path loss would be proportional only to the distance between the Tx and the Rx. These factors highly influence the distribution of the E-field in the environment, generating E-field values with more variables in [21] and [28] than in our case. As a consequence, the o-kriging technique estimates with less accuracy E-fields that rapidly change in space (as happened in [21] and [28]).

Martínez-González et al. [29] used o-kriging interpolation to generate an indoor exposure map for the E-field generated by three Wi-Fi routers at 2.45 GHz. The E-field values used for training and validating the kriging techniques were collected with experimental measures. The RMSE and MAE relative to the maximum E-field were found to be 4.2% and 3.9%, respectively. These errors were significantly lower than those obtained in our study, i.e., relative RMSE of 13%–16.2% and relative MAE of 10%–12% across the different scenarios, meaning that o-kriging in [29] performed with more accuracy than in our case. These results were expected, as the indoor scenario investigated by [29] was simpler in terms of propagation compared to the vehicular urban scenarios here considered. Indeed, the smaller number of Tx considered and the smaller dimension of the indoor scenario (0.9×10^{-3} km^2) with respect to our (0.039 km^2) generates lower variability of the E-field distribution than in our case. Thus, o-kriging performed better in [29] than in our study.

V. CONCLUSION

In this study, we designed an analytical approach based on o-kriging and co-kriging spatial interpolation techniques to estimate the E-field values generated in realistic V2X vehicular urban scenarios by V2V and V2I communication technologies operated at 5.9 GHz. This approach allowed us to obtain E-field values in the analyzed urban area with high accuracy and low computational effort, thus overcoming the main disadvantages of experimental measures (such as time, cost, and implementation effort) and deterministic methods (such as memory and time consumption). Specifically, the proposed approach allows us to reduce computational time by up to 87%. Both o-kriging and co-kriging provide very good accuracy in estimating E-field values in vehicular scenarios, reaching an accuracy of 97% in the simplest scenario and 89% in the most complex scenario; the errors were generally low. We found that the accuracy of the co-kriging analysis did not improve with an increase in the number of covariables. Finally, we obtained good accuracy also when considering the contribution of the DS effect to the total E-field.

This analytical approach can be employed, as the next step, to develop large datasets for training artificial neural networks (ANNs).

APPENDIX A
SPATIAL CORRELATION ANALYSIS

The following are the equations to perform the spatial correlation analysis in o-kriging and co-kriging approaches. In o-kriging, the spatial correlation analysis is obtained by calculating the experimental variogram $\gamma*(\mathrm{h})$ through the following equation [51]:

$$\gamma^*(h) = \frac{1}{2N(h)} \sum_{i=1}^{N(h)} [Z(x_i) - Z(x_i + h)]^2 \tag{A1}$$

where Z represents the primary feature of the E-field values; h is the lag distance (i.e., the distance between each pair of Rx); N(h) is the number of Rx pairs separated by lag distance h; and $Z(x_i)$ and $Z(x_i + h)$ are the values of the E-field at a spatial location x_i and $x_i + h$, respectively. For simplicity, we refer to the term variogram with $\gamma(h)$ even if it is generally denoted as $2\gamma(h)$. In co-kriging, instead, it is necessary to calculate an experimental variogram for each covariable considered. For instance, when considering only one covariable [i.e., the *distance between* Tx-Rx denoted as $Y(x_i)$] in addition to the

primary feature [E-field, Z(X_i)], the experimental variogram functions are defined by these equations

$$\gamma^*_{ZZ}(h) = \frac{1}{2N(h)} \sum_{i=1}^{N(h)} [Z(x_i) - Z(x_i + h)]^2 \quad \text{(A2)}$$

$$\gamma^*_{YY}(h) = \frac{1}{2N(h)} \sum_{i=1}^{N(h)} [Y(x_i) - Y(x_i + h)]^2 . \quad \text{(A3)}$$

The variogram was estimated under the assumption of second-order stationarity, i.e., the mean and covariance of Z(x) are stationary in time. Furthermore, the co-kriging, in addition to the variograms (A2) and (A3), also calculated the cross-covariance [from the variograms (A2) and (A3)] and used it to derive the cross-variogram as a function of the lag distance h. This was possible because, under the assumption of second-order stationarity, the cross-covariance and the cross-variogram are related by the formula: $\gamma_{ZY}(h) = C_{ZY}(0) - C_{ZY}(h)$ [24]. With the cross-variogram, it was possible to obtain the spatial relation between the multiple features (primary and secondary features). The equation of the cross-variogram is

$$\gamma^*_{ZY}(h) = \frac{1}{2N(h)} \sum_{i=1}^{N(h)} [Z(x_i) - Z(x_i + h)]\,[Y(x_i) - Y(x_i + h)]. \quad \text{(A4)}$$

Appendix B
Spatial Interpolation Analysis

In this section, we reported the equations for the estimation of the unknown E-field values. In o-kriging, the unknown values are weighted over a linear combination of sample values where the weights are determined from the variogram by minimizing the variance of the estimated values.

Being $Z^*(x_0)$ the estimated value of the unknown E-field at the position x_0, $Z^*(x_0)$ is calculated with the formula as follows:

$$Z^*(x_o) = \sum_{i=1}^{n} \lambda_i Z(x_i) \quad \text{(A5)}$$

meaning that $Z^*(x_0)$ at the position x_0 is estimated by the weighted sum of the known n-point sampling values. In (A5), $Z(x_i)$ is the E-field value at the spatial point x_i, n is the number of samples inside the *range* of influence of the variogram, and λ_i (with i = 1, 2, . . . , n) is the o-kriging weight coefficient to be determined. As a clarification, we revisit here the meaning of *range*, i.e., the maximum lag distance (h) within which there is a correlation between each pair of Rx. Imposing the estimation to be unbiased and assuming the second-order stationarity condition, the following requirement must be satisfied:

$$\sum_{i=1}^{n} \lambda_i = 1. \quad \text{(A6)}$$

To determine the weight coefficients in (A5) by minimizing the estimate variation [53], o-kriging computes the estimated variance to have the lowest estimation error variance possible at x_0

$$\sigma^2_E(x_0) = Var\left[Z^*(x_0) - Z(x_o)\right]. \quad \text{(A7)}$$

By minimizing (A7), with the constraint of unbiased (A6) introduced by an additional Lagrange parameter μ, the kriging equation for computing λ_i and μ coefficients is obtained [54], [55], [56]

$$\sum_{i=1}^{n} \lambda_i \cdot \gamma(x_i, x_j) + \mu = \gamma(x_0, x_i), \quad j = 1, 2, 3, \ldots, n \quad \text{(A8)}$$

where γ is the theoretical variogram fit to the previously defined (A1) in Appendix A. By solving (A8), it is possible to obtain the weight coefficients λ_i and use them in (A5) to calculate the estimated E-field values in the unknown sample points [$Z^*(x_0)$]. The co-kriging estimator, instead, differently from o-kriging (A5), is written as

$$Z^*(x_o) = \sum_{i=1}^{n} \lambda_i Z(x_i) + \sum_{j=1}^{m} \lambda'_j Y(x_j) \quad \text{(A9)}$$

where λ_i and λ'_j are the co-kriging weight coefficients for the primary feature and the secondary feature, respectively; and n and m are the number of samples inside the *ranges* of the variogram for the primary and secondary features, respectively. To get an estimation that is unbiased, the following requirements must be respected:

$$\sum_{i=1}^{n} \lambda_i + \sum_{j=1}^{m} \lambda'_j = 1. \quad \text{(A10)}$$

This constraint (A10) brings the introduction of only one Lagrange parameter μ, developing this system of equations for computing the co-kriging weight coefficients (λ_i and λ_j)

$$\sum_{i=1}^{n} \lambda_i \cdot C_{ZZ}(x_a - x_j) + \sum_{j=1}^{m} \lambda'_j C_{ZY}(x_a - x'_j) + \mu = C_{ZZ}(x_a - x_0), \quad a = 1, 2, 3, \ldots, n \quad \text{(A11)}$$

$$\sum_{i=1}^{n} \lambda_i \cdot C_{YZ}(x'_b - x_i) + \sum_{j=1}^{m} \lambda'_j C_{YY}(x_b - x'_j) + \mu = C_{YZ}(x'_b - x_0), \quad b = 1, 2, 3, \ldots, n \quad \text{(A12)}$$

where C represents the cross-covariance used to compute the cross-variogram (A4). By solving (A11) and (A12), it was possible to obtain the co-kriging weight coefficients (λ_i and λ'_j); and by applying them in (A9), the co-kriging computed the estimated E-field values in the unknown sample points [$Z^*(x_0)$]. Please note that the formulas (A9)–(A12) hold when the co-kriging considers only one covariable; when more covariables are considered, the co-kriging adds as many terms and weight coefficients in the formulas as the number of covariables that were considered.

References

[1] K. Sjoberg, P. Andres, T. Buburuzan, and A. Brakemeier, "Cooperative intelligent transport systems in Europe: Current deployment status and outlook," *IEEE Veh. Technol. Mag.*, vol. 12, no. 2, pp. 89–97, Jun. 2017, doi: 10.1109/MVT.2017.2670018.

[2] X. Shen, R. Fantacci, and S. Chen, "Internet of Vehicles [scanning the issue]," *Proc. IEEE*, vol. 108, no. 2, pp. 242–245, Feb. 2020, doi: 10.1109/JPROC.2020.2964107.

[3] J. Wang, Y. Shao, Y. Ge, and R. Yu, "A survey of vehicle to everything (V2X) testing," *Sensors*, vol. 19, no. 2, p. 334, Jan. 2019, doi: 10.3390/s19020334.

[4] IEEE Standard for Information Technology-Telecommunications and Information Exchange Between Local and Metropolitan Area Networks-Specific Requirements, Part 11: Wireless LAN Medium Access Control (MAC) and Physical Layer (PHY) Specifications Amendment 6: Wireless Access in Vehicular Environments, Standard 802.11p, 2010.

[5] Intelligent Transport Systems (ITS); LTE-V2X Access Layer Specification for Intelligent Transport Systems Operating in the 5 GHz Frequency Band, Standard ETSI EN 303 613, V1.1.1, 2020.

[6] Technical Specification Group Radio Access Network; Study on LTE Based V2X Services; (Release 14), Standard TR 36.885, V14.0.0, 3GPP, 2016.

[7] Technical Specification Group Radio Access Network; V2X Services Based on NR; User Equipment (UE) Radio Transmission and Reception (Release 16), Standard TR 38.886, V16.3.0, 3GPP, 2021.

[8] Technical Specification Group Radio Access Network; NR Sidelink Enhancement; User Equipment (UE) Radio Transmission and Reception (Release 17), Standard TR 38.785, V0.5.0, 3GPP, 2021.

[9] (2021). *5GAA Automotive Association, Deployment Band Configuration for C-V2X At 5.9 GHz in Europe, in Position Paper*. [Online]. Available: https://5gaa.org/content/uploads/2021/06/5GAA_S-210019_Positionpaper-on-European-deployment-band-configuration-for-C-V2X_final.pdf

[10] G. Ziegelberger et al., "Guidelines for limiting exposure to electromagnetic fields (100 kHz to 300 GHz)," *Health Phys.*, vol. 118, no. 5, pp. 483–524, 2020, doi: 10.1097/HP.0000000000001210.

[11] G. Tognola et al., "Survey of exposure to RF electromagnetic fields in the connected car," *IEEE Access*, vol. 10, pp. 47764–47781, 2022, doi: 10.1109/ACCESS.2022.3170035.

[12] C. K. Anjinappa and I. Guvenc, "Millimeter-wave V2X channels: Propagation statistics, beamforming, and blockage," in *Proc. IEEE 88th Veh. Technol. Conf. (VTC-Fall)*, Aug. 2018, pp. 1–6, doi: 10.1109/VTCFall.2018.8690733.

[13] B. Antonescu, M. T. Moayyed, and S. Basagni, "Diffuse scattering models for mmWave V2X communications in urban scenarios," in *Proc. Int. Conf. Comput., Netw. Commun. (ICNC)*, Honolulu, HI, USA, Feb. 2019, pp. 923–929, doi: 10.1109/ICCNC.2019.8685661.

[14] M. Benini, S. Gallucci, M. Bonato, M. Parazzini, and G. Tognola, "Evaluation of road user radio-frequency exposure levels in an urban environment from vehicular antennas and the infrastructure in ITS-G5 5.9 GHz communication," *IEEE Access*, vol. 12, pp. 51419–51430, 2024, doi: 10.1109/ACCESS.2024.3385664.

[15] G. Tognola, M. Benini, M. Bonato, S. Gallucci, and M. Parazzini, "Assessment of the variability of human exposure to radiofrequency electromagnetic fields arising from 5.9 GHz vehicular communication in urban environments," *Sensors*, vol. 23, no. 15, p. 6802, Jul. 2023, doi: 10.3390/s23156802.

[16] R. C. Dwarakanath, J. D. Naranjo, and A. Ravanshid, "Modeling of interference maps for licensed shared access in LTE-advanced networks supporting carrier aggregation," in *Proc. IFIP Wireless Days (WD)*, Valencia, Spain, Nov. 2013, pp. 1–6, doi: 10.1109/WD.2013.6686457.

[17] S. Üreten, A. Yongaçoğlu, and E. Petriu, "A comparison of interference cartography generation techniques in cognitive radio networks," in *Proc. IEEE Int. Conf. Commun. (ICC)*, Jun. 2012, pp. 1879–1883, doi: 10.1109/ICC.2012.6364111.

[18] D. Denkovski, V. Atanasovski, L. Gavrilovska, J. Riihijärvi, and P. Mähönen, "Reliability of a radio environment map: Case of spatial interpolation techniques," in *Proc. IEEE 7th Int. ICST Conf. Cogn. Radio Orient. Wireless Netw. Commun. (CROWNCOM)*, Jun. 2012, pp. 248–253, doi: 10.4108/ICST.CROWNCOM.2012.248452.

[19] H. B. Yilmaz and T. Tugcu, "Location estimation-based radio environment map construction in fading channels," *Wireless Commun. Mobile Comput.*, vol. 15, no. 3, pp. 561–570, Feb. 2015, doi: 10.1002/wcm.2367.

[20] N. Cressie, *Statistics for Spatial Data*. New York, NY, USA: Wiley, 1993.

[21] M. A. Azpurua and K. D. Ramos, "A comparison of spatial interpolation methods for estimation of average electromagnetic field magnitude," *Progr. Electromagn. Res.*, vol. 14, pp. 135–145, Sep. 2010.

[22] M. Rufo, A. Antolín, J. M. Paniagua, and A. Jiménez, "Optimization and comparison of three spatial interpolation methods for electromagnetic levels in the AM band within an urban area," *Environ. Res.*, vol. 162, pp. 219–225, Apr. 2018, doi: 10.1016/j.envres.2018.01.014.

[23] Z. Han, J. Liao, Q. Qi, H. Sun, and J. Wang, "Radio environment map construction by Kriging algorithm based on mobile crowd sensing," *Wireless Commun. Mobile Comput.*, vol. 2019, pp. 1–12, Feb. 2019, doi: 10.1155/2019/4064201.

[24] G. Matheron, "Principles of geostatistics," *Econ. Geol.*, vol. 58, no. 8, pp. 1246–1266, Dec. 1963.

[25] P. De Doncker, J.-M. Dricot, R. Meys, M. Hélier, and W. Tabbara, "Electromagnetic fields estimation using spatial statistics," *Electromagnetics*, vol. 26, no. 2, pp. 111–122, Feb. 2006, doi: 10.1080/02726340500486450.

[26] J. M. Paniagua, M. Rufo, A. Jimenez, and A. Antolin, "The spatial statistics formalism applied to mapping electromagnetic radiation in urban areas," *Environ. Monitor. Assessment*, vol. 185, no. 1, pp. 311–322, Jan. 2013, doi: 10.1007/s10661-012-2555-7.

[27] R. Ramirez-Vazquez, I. Escobar, J. J. H. Moreno, A. Martínez-Plaza, S. Maffey, and E. Arribas, "Personal exposure from free Wi-Fi hotspots in downtown Mexico city," *Environ. Sci. Pollut. Res.*, vol. 30, no. 39, pp. 91216–91225, Jul. 2023, doi: 10.1007/s11356-023-28839-5.

[28] S. Aerts, D. Deschrijver, L. Verloock, T. Dhaene, L. Martens, and W. Joseph, "Assessment of outdoor radiofrequency electromagnetic field exposure through hotspot localization using kriging-based sequential sampling," *Environ. Res.*, vol. 126, pp. 184–191, Oct. 2013, doi: 10.1016/j.envres.2013.05.005.

[29] A. Martínez-González, J. Monzó-Cabrera, A. J. Martínez-Sáez, and A. J. Lozano-Guerrero, "Minimization of measuring points for the electric field exposure map generation in indoor environments by means of Kriging interpolation and selective sampling," *Environ. Res.*, vol. 212, Sep. 2022, Art. no. 113577, doi: 10.1016/j.envres.2022.113577.

[30] S. Schiesl, T. Kopacz, and D. Heberling, "Towards a crowdsourcing-based EMF exposure monitoring: Evaluation of smartphone measurements using kriging," in *Proc. 15th Eur. Conf. Antennas Propag. (EuCAP)*, Dusseldorf, Germany, Mar. 2021, pp. 1–5, doi: 10.23919/EUCAP51087.2021.9410984.

[31] S. Roger, C. Botella, J. J. Pérez-Solano, and J. Perez, "Application of radio environment map reconstruction techniques to platoon-based cellular V2X communications," *Sensors*, vol. 20, no. 9, p. 2440, Apr. 2020.

[32] V. Chowdappa, C. Botella, J. J. Samper-Zapater, and R. J. Martinez, "Distributed radio map reconstruction for 5G automotive," *IEEE Intell. Transp. Syst. Mag.*, vol. 10, no. 2, pp. 36–49, Summer 2018, doi: 10.1109/MITS.2018.2806632.

[33] M. Knotters, D. J. Brus, and J. H. O. Voshaar, "A comparison of kriging, co-kriging and Kriging combined with regression for spatial interpolation of horizon depth with censored observations," *Geoderma*, vol. 67, nos. 3–4, pp. 227–246, Aug. 1995, doi: 10.1016/0016-7061(95)00011-c.

[34] G. Tognola et al., "Numerical assessment of RF human exposure in smart mobility communications," *IEEE J. Electromagn., RF Microw. Med. Biol.*, vol. 5, no. 2, pp. 100–107, Jun. 2021, doi: 10.1109/JERM.2020.3009856.

[35] M. Benini et al., "Road user exposure from ITS-5.9 GHz vehicular connectivity," *Sensors*, vol. 22, no. 18, p. 6986, Sep. 2022, doi: 10.3390/s22186986.

[36] M. Benini et al., "Assessment of Children's exposure to intelligent transport system 5.9 GHz vehicular connectivity using numerical dosimetry," *Sensors*, vol. 23, no. 11, p. 5170, May 2023, doi: 10.3390/s23115170.

[37] F. A. Rodríguez-Corbo et al., "Deterministic 3D ray-launching millimeter wave channel characterization for vehicular communications in urban environments," *Sensors*, vol. 20, no. 18, p. 5284, Sep. 2020, doi: 10.3390/s20185284.

[38] M. Gallo, S. Bruni, M. Pannozzo, and D. Zamberlan, "Performance evaluation of C2C antennas on car body," in *Proc. 7th Eur. Conf. Antennas Propag. (EuCAP)*, Apr. 2013, pp. 3136–3139.

[39] *Study on Evaluation Methodology of New Vehicle-to-Everything(V2X) Use Cases for LTE and NR*, document TR 37.885, V15.3.0, 3GPP, Jun. 2019.

[40] Autotalks.(2020). *Cost-Efficient C-V2X Antenna Installation*. Accessed: Mar. 6, 2024. [Online]. Available: https://auto-talks.com/wp-content/uploads/2021/07/Cost-efficient-CV2X-Antenna-Installation-final.pdf

[41] K. K. Katare, I. M. Yousaf, and B. K. Lau, "Challenges and solutions for antennas in vehicle-to-everything services," *IEEE Commun. Mag.*, vol. 60, no. 1, pp. 52–58, Jan. 2022, doi: 10.1109/MCOM.001.2100572.

[42] *Effects of Building Materials and Structures on Radiowave Propagation Above About 100 MHz*, document ITU-R 2040, 2015.

[43] M. Boban, J. Barros, and O. K. Tonguz, "Geometry-based vehicle-to-vehicle channel modeling for large-scale simulation," *IEEE Trans. Veh. Technol.*, vol. 63, no. 9, pp. 4146–4164, Nov. 2014, doi: 10.1109/TVT.2014.2317803.

[44] Remcom.(2021). *Wireless InSite 3D Wireless Prediction Software*. Accessed: Mar. 5, 2024. [Online]. Available: http://www.remcom.com/wirelessinsite-em-propagation-software

[45] D. Solomitckii et al., "Characterizing the impact of diffuse scattering in urban millimeter-wave deployments," *IEEE Wireless Commun. Lett.*, vol. 5, no. 4, pp. 432–435, Aug. 2016, doi: 10.1109/LWC.2016.2580669.
[46] V. Degli-Esposti, F. Fuschini, E. M. Vitucci, and G. Falciasecca, "Measurement and modelling of scattering from buildings," *IEEE Trans. Antennas Propag.*, vol. 55, no. 1, pp. 143–153, Jan. 2007, doi: 10.1109/TAP.2006.888422.
[47] V. Degli-Esposti and H. L. Bertoni, "Evaluation of the role of diffuse scattering in urban microcellular propagation," in *Proc. 21st Century Commun. Village, VTC-Fall, IEEE VTS 50th Veh. Technol. Conf.*, May 1999, pp. 1392–1396, doi: 10.1109/VETECF.1999.801491.
[48] E. M. Vitucci, F. Mani, V. Degli-Esposti, and C. Oestges, "Study of a polarimetric model for diffuse scattering in urban environment," in *Proc. 6th Eur. Conf. Antennas Propag. (EUCAP)*, Mar. 2012, pp. 39–43, doi: 10.1109/EuCAP.2012.6206681.
[49] M. E. Rossi and C. V. Deutsch, *Mineral Resource Estimation*. Cham, Switzerland: Springer, 2013.
[50] J. Allaire, "RStudio: Integrated development environment for R," *Boston, MA*, vol. 770, no. 394, pp. 165–171, 2012.
[51] D. E. Myers, "Matrix formulation of co-kriging," *J. Int. Assoc. Math. Geol.*, vol. 14, no. 3, pp. 249–257, Jun. 1982, doi: 10.1007/bf01032887.
[52] M. J. Pyrcz and C. V. Deutsch, *Geostatistical Reservoir Modeling*. London, U.K.: Oxford Univ. Press, 2014.
[53] N. Cressie, *Statistics for Spatial Data*. Hoboken, NJ, USA: Wiley, 2015.
[54] J. P. Chils and P. Delfiner, *Geostatistics, Modeling Spatial Uncertainty*. Hoboken, NJ, USA: Wiley, 1999.
[55] M. L. Stein, *Interpolation of Spatial Data: Some Theory for Kriging*. New York, NY, USA: Springer, 1999.
[56] H. Wackernagel, *Multivariate Geostatistics, an Introduction With Applications*. New York, NY, USA: Springer, 1995.
[57] Y. O. Isselmou, H. Wackernagel, W. Tabbara, and J. Wiart, "Geostatistical estimation of electromagnetic exposure," in *GeoENV VI–Geostatistics for Environmental Applications*. Amsterdam, The, Netherlands: Springer, Mar. 2008, pp. 59–70.

Martina Benini received the master's degree in biomedical engineering and the Ph.D. degree in bioengineering from Politecnico di Milano, Milan, Italy, in 2020 and 2024, respectively.

She is currently a Research Scientist with the Institute of Electronics, Information Engineering and Telecommunication (IEIIT), Consiglio Nazionale delle Ricerche (CNR), Milan. Her research interests are related to the study of the interaction between the electromagnetic field (EMF) and the human body with deterministic and stochastic methods.

Silvia Gallucci received the master's degree in biomedical engineering from the University of Pisa, Pisa, Italy, in 2019, and the Ph.D. degree in bioengineering from Politecnico di Milano, Milan, Italy, in 2023, with a focus on EMF interactions.

In January 2024, she was a Research Scientist with the Institute of Electronics, Computer and Telecommunication Engineering, Consiglio Nazionale delle Ricerche, Milan. Her main research interests include exposure assessment of electromagnetic fields with numerical dosimetry and particularly from 5G mobile communication.

Samuel Goegebeur received the M.Sc. degree in engineering physics from Ghent University, Ghent, Belgium, in 2022, where he is currently pursuing the Ph.D. degree in 5G spatiotemporal exposure modeling with the Department of Information Technology, WAVES Group.

He joined WAVES Group, Department of Information Technology, Ghent University, in 2022. His research interests include raytracing simulations for geostatistical 5G exposure modeling and in situ electromagnetic field exposure measurement campaigns.

Marta Parazzini (Member, IEEE) is currently a Research Scientist with the Institute of Electronics, Computer and Telecommunication Engineering, Italian National Research Council, Milan, Italy.

Her current research interests include the study of the interactions of EMF with biological systems, deterministic and stochastic computational dosimetry, and medical applications of EMF, particularly techniques for noninvasive brain stimulation.

Wout Joseph (Senior Member, IEEE) was born in Ostend, Belgium, in October 1977. He received the M.Sc. degree in electrical engineering and the Ph.D. degree from Ghent University, Ghent, Belgium, in July 2000 and March 2005, respectively.

From 2007 to 2012, he was a Post-Doctoral Fellow with the Research Foundation Flanders (FWO-V), Brussels, Belgium. Since October 2009, he has been a Professor of experimental characterization of wireless communication systems. He has been a PI with IMEC, Ghent, since 2017. His Ph.D. work dealt with measuring and modeling electromagnetic fields around base stations for mobile communications related to the health effects of exposure to electromagnetic radiation. His professional interests are electromagnetic field exposure assessment, propagation for wireless communication system antennas, and calibration. Furthermore, he specializes in wireless performance analysis and quality of experience.

Gabriella Tognola received the master's degree in electronic engineering and the Ph.D. degree in bioengineering from Politecnico di Milano, Milan, Italy, in 1993 and 1998, respectively.

She is currently a Senior Research Scientist with the Institute of Electronics, Computer and Telecommunication Engineering, Consiglio Nazionale delle Ricerche, Milan. Her main research interests include exposure assessment of electromagnetic fields with numerical dosimetry and machine learning methods, and modeling of electromagnetic fields for biomedical applications.